*J. Fluid Mech.* (2003), *vol.* 478, *pp.* 125–134.  
DOI: 10.1017/S0022112002003427 Printed in the United Kingdom

# Air entrapment under an impacting drop

By S. T. THORODDSEN[1], T. G. ETOH[2] AND K. TAKEHARA[2]

[1]Mechanical Engineering, National University of Singapore, 9 Engineering Drive 1, Singapore 117576

[2]Civil and Environmental Engineering, Kinki University, Higashi-Osaka 577-8502, Japan

(Received 10 October 2002 and in revised form 22 November 2002)

When a drop impacts on a liquid surface it entraps a small amount of air under its centre as the two liquid surfaces meet. The contact occurs along a ring enclosing a thin disk of air. We use the next-generation ultra-high-speed video camera, capable of 1 million f.p.s. (Etoh *et al.* 2002), to study the dynamics of this air sheet as it contracts due to surface tension, to form a bubble or, more frequently, splits into two bubbles. During the contraction of the air disk an azimuthal undulation, resembling a pearl necklace, develops along its edge. The contraction speed of the sheet is accurately described by a balance between inertia and surface tension. The average initial thickness of the air sheet decreases with higher impact Reynolds numbers, becoming less than one micron. The total volume of air entrapped depends strongly on the bottom curvature of the drop at impact. A sheet of micro-bubbles is often observed along the original interface. Oguz–Prosperetti bubble rings are also observed. For low Weber numbers ($We < 20$) a variety of other entrapment phenomena appear.

## 1. Introduction

Raindrops are known to entrain air bubbles into the surface layers of lakes and other bodies of water, representing one mechanism for the transport of gas from the atmosphere into the ocean, see for example Blanchard & Woodcock (1957) and experiments by Esmailizadeh & Mesler (1986). Bursting of such bubbles at the ocean surface can generate micron-sized drops which evaporate to form small salt crystals, which can in turn serve as nucleation sites in clouds. Gas entrapment by impacting drops is also important in a number of industrial processes. In chemical processes, such bubbles can transport surface contaminants into the bulk liquid. Small bubbles are also important during boiling as they can serve as nucleation sites. Drops ejected out of the boiling liquid can thereby enhance the boiling rate, by entrapping micro-bubbles as they fall back onto the liquid surface. Oscillations of trapped bubbles are known to produce the characteristic underwater noise of rain, as reviewed by Prosperetti & Oguz (1993). The collisions of drops are also relevant to the growth of raindrops in clouds, e.g. Foote (1975), Jiang, Umemura & Law (1992) and Nobari, Jan & Tryggvason (1996).

Theoretical work on this phenomenon has mostly been limited to lower Reynolds numbers of relevance to emulsions, e.g. Rother, Zinchenko & Davis (1997), or to asymptotic studies at smaller Weber numbers focusing on the rebounding of nearly spherical drops, most recently by Gopinath & Koch (2002). Here we use a novel ultra-high-speed video camera to study the details of air entrapment in the parameter range of typical raindrops. These results can help in estimating the amount of air entrained into lakes and the ocean by rain.

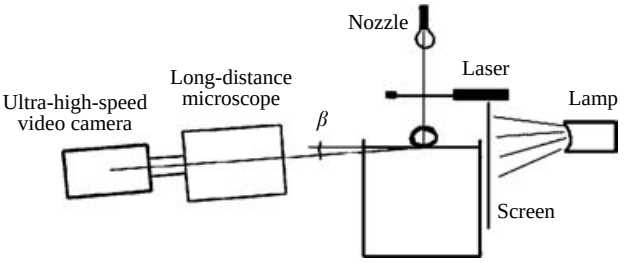


FIGURE 1. Experimental setup, not to scale.

## 2. Experimental setup

Figure 1 shows the overall setup of the experiment. The liquid pool is contained in a small glass container ($5 \times 5 \times 7$ cm). A long-distance microscope (Questar QM100) is used to magnify the impact region, looking horizontally slightly upwards along the free surface, at an angle $\beta$ of 1°. Deionized water drops are generated by a gravity-driven pinch-off from a circular nozzle, cut from a steel syringe-needle. Triggering is achieved by the drop blocking a laser beam during its fall. Diffuse backlighting is produced by a high-intensity lamp (Photron HVC-SL), illuminating a thin sheet of drafting paper. The air sheet becomes visible due to the index of refraction difference between air and water, usually forming a dark region in the field of view.

### 2.1. *Ultra-high-speed video camera*

The initial deformation and contact of the liquid surfaces, during drop impacts, occurs extremely rapidly making the study of air entrapment challenging. Observations at the relevant parameter regimes have not been accessible until now. To capture the dynamics of the trapped air sheet we use a newly developed ultra-high-speed video camera (Etoh *et al.* 2002), capable of up to 1 million frames/s. To achieve this very high frame rate the camera uses simultaneously parallel recording of all pixels, along with In-Situ Image Storage (ISIS) next to every pixel on the CCD chip. The pure CCD design implements smoothly curved storage channels for low-noise operation and 10-bit intensity resolution. This minimizes electronic noise generated by the sharp turns universally employed in previous CCD designs. The prototype can acquire 103 consecutive frames, an order of magnitude more than previous cameras, giving it unparallel flexibility. Each frame has $260 \times 312$ pixel elements irrespective of the frame rate used. The resulting image quality is far superior to the very popular CMOS cameras developed earlier by Etoh (1992), where the number of pixels was reduced to $64 \times 64$ at the highest frame-rate of 40 500 f.p.s. The new camera records frames continually into the ISIS memory, which clears through a drain, until a trigger signal stops the imaging. This signal can be timed at any of the 103 images, giving the needed flexibility to the external trigger. This is essential when studying phenomena whose onset may be subject to temporal jitter. The movie clips are then rapidly stored onto a dedicated computer, freeing the sensor for the next experiment. This flexibility and ease of use is essential when investigating phenomena, such as drop impacts, which have wide parameter range, allowing numerous experiments in rapid succession.

## 3. Results

Figure 2 shows typical entrapment events for a drop of deionized water. It shows the entrapped air sheet and its rapid contraction into a vertical column of air, which

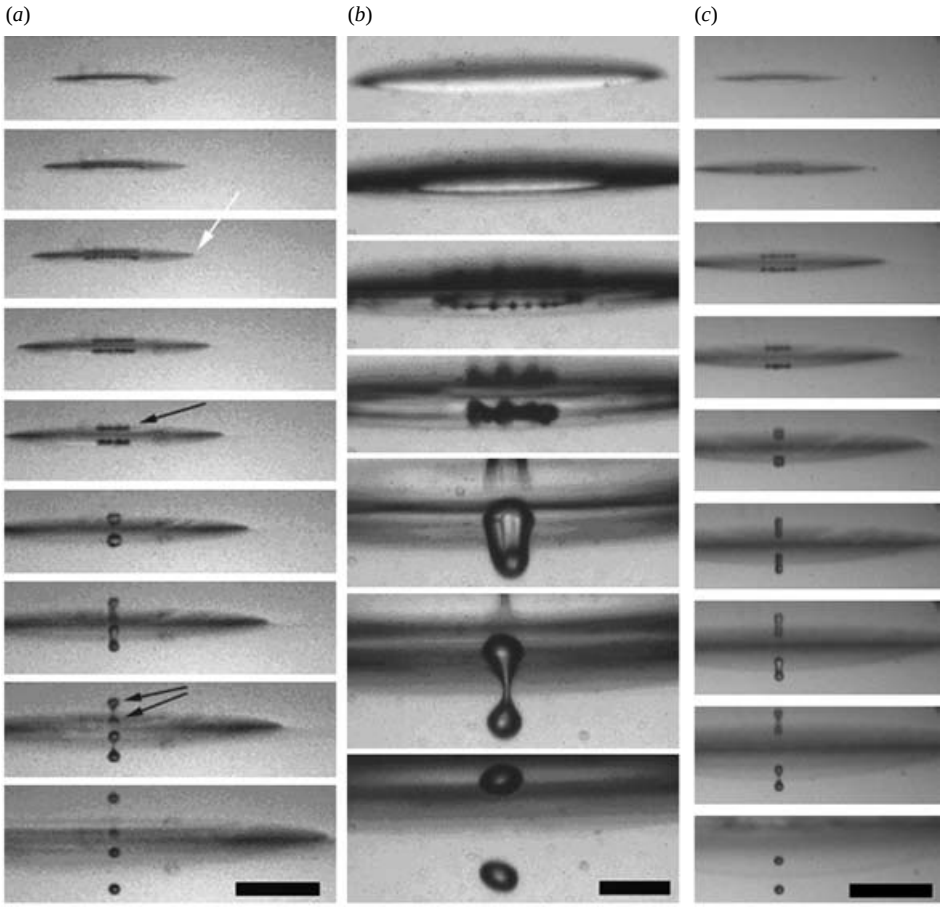


FIGURE 2. Selected frames from a typical video clip, showing the air sheet captured under an impacting drop, as it contracts and splits into two bubbles. (*a*) $D = 3.47$ mm, $U = 1.54\,\mathrm{m\,s^{-1}}$ ($We = 115$, $Re_g = 356$). Taken from a 200 kHz sequence, 10, 15, 20, 30, 40, 65, 90, 110 and 185 μs after $T_o$. (*b*) $D = 4.24$ mm, $U = 0.49\,\mathrm{m\,s^{-1}}$ ($We = 14$, $Re_g = 138$), from a sequence taken at 20 kHz, 50, 150, 250, 400, 950, 1250 and 1550 μs after $T_o$. This sequence is taken with $\beta = 7^\circ$ to highlight the azimuthal necklace instability. (*c*) Results for higher impact velocity, $U = 2.41\,\mathrm{m\,s^{-1}}$, $D = 3.47$ mm ($We = 282$, $Re_g = 556$), 10, 20, 30, 40, 60, 80, 100, 130 and 190 μs after $T_o$. The scale bars are 500 μm long. The duplicate images, marked by representative black arrows, are reflections in the liquid surface.

splits into two bubbles. It also shows the outwards motion of the contact line between the drop and the pool (marked by the white arrow). The contracting sheet of air appears unstable to azimuthal capillary instability, as bumps are clearly visible along the edge in figure 2(*b*), but the edge does not break up into bubbles, as shown below. Occasionally the sheet forms only one bubble, or breaks up into four bubbles due to this azimuthal instability.

### 3.1. *Drop shapes and the volume of entrained air*

The amount of entrapped air depends strongly on the impact Reynolds number based on impact velocity $U$, $Re_g = DU/\nu_g$, as well as the bottom shape of the drop at the instant it hits the liquid surface. Most of the results shown here are for the same drop size, $D = 3.47$ mm, but varying release heights. The resulting impact Reynolds

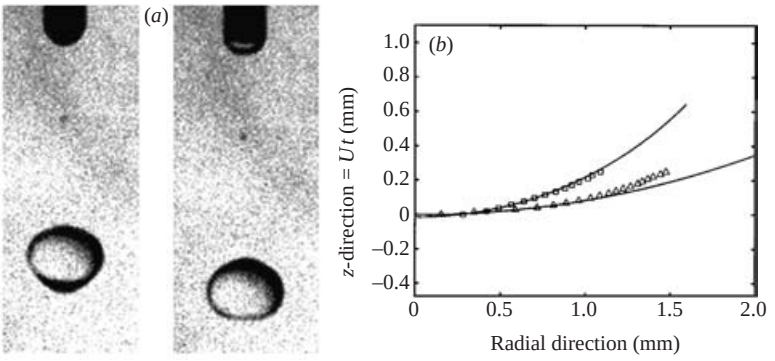


FIGURE 3. (*a*) Drop during free fall showing typical variations in shape and bottom curvature. The needle diameter is 2.45 mm, producing a drop 4.24 mm in diameter. (*b*) Drop shapes deduced from the outwards motion of the outer contacts between drop and pool liquid, marked by the white arrow in figure 2(*a*). Results are shown for $D = 3.47$ mm and impact heights $H = 2.75$ cm (△) and $H = 75.4$ cm (□).

numbers are between 120 and 900 based on the kinematic viscosity of air, $\nu_g$. The liquid Reynolds numbers $Re_l$ are 15 times higher. The corresponding liquid Weber numbers, $We = \rho D U^2/\sigma$, are between 20 and 700. Owing to these high Weber numbers, the drop exhibits large shape oscillations during its fall, especially immediately after the release from the nozzle. Figure 3(*a*) shows representative drop shapes. The bottom shape of the drop can be characterized by a radius of curvature. One measure of this radius is obtained directly from the video images by looking at the outwards motion of the outer contact between drop and pool liquid, marked by a white arrow in figure 2(*a*). This contact will move out radially faster during the impact of a flat drop, than for a more 'pointed' drop. Figure 3(*b*) shows this indication of the drop shape for the two extreme cases observed herein. The solid curves in figure 3(*b*) represent inscribed circles of radius $R_b$. The vertical coordinate is estimated by using the impact velocity $Ut$. Figure 4(*a*) shows the correspondence between the original diameter of the trapped air disk and this bottom radius of curvature $R_b$, both normalized by the drop diameter. The initial thickness $\delta$ of the air sheet, as the drop makes first contact, can be obtained by measuring the total volume of the bubbles and maximum diameter of the sheet. Figure 4(*b*) shows this thickness $\delta$ as a function of the impact Reynolds number, where the important viscosity is here the air viscosity. The large variation in $\delta$ for the lowest impact velocities is due to the large shape oscillations as discussed above. The thickness reduces approximately linearly with increasing impact velocity suggesting that for even higher $Re_g$ the sheet may break up before it can contract into a bubble.

One can obtain a rough estimate of $\delta$, based on the thickness of the boundary layers in the air flow along the gap between the liquid surface, which is driven by the stagnation pressure at the underside of the drop. This thickness grows as $\delta \approx \sqrt{\nu_g T}$ where $T$ is the viscous-dominated duration of the impact. If one estimates $T \approx \delta/U$ then $\delta^2 \approx \nu_g \delta/U$ or $\delta \approx \nu_g/U \approx 4\,\mu$m (for $U = 4\,\mathrm{m\,s^{-1}}$), which is larger than, but of the same order of magnitude, as the measured values.

### 3.2. *Contraction speed*

The contraction speed of the entrapped air sheet is principally determined by its thickness. Oguz & Prosperetti (1989) showed numerically, for an idealized case, that

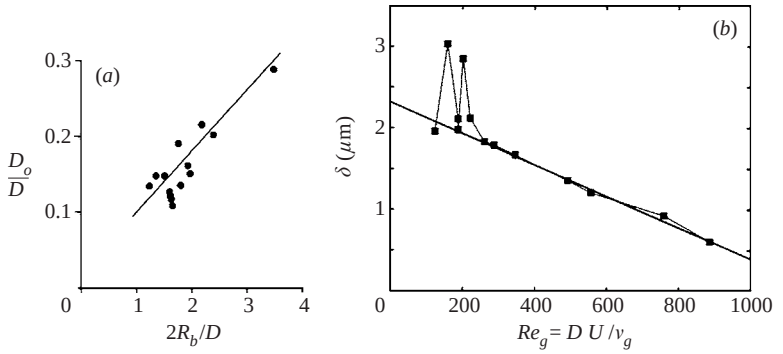


FIGURE 4. (*a*) The initial diameter of entrapped air disk $D_o$ vs. bottom radius of curvature $R_b$, normalized by drop diameter $D = 3.47$ mm. (*b*) The average initial thickness $\delta$ of the air sheet vs. Reynolds number of the air flow $Re_g$ ($D = 3.47$ mm).

the normalized speed of the edge of a two-dimensional sheet of air is approximately constant. In addition to $\delta$, the liquid density $\rho$ and surface tension $\sigma$ are used in this normalization, i.e. the velocity $u = C\sqrt{\sigma/(\rho\delta)}$, where $C$ is a constant taking a value of approximately 1. Based on this we can construct a simple model of the contraction speed. We assume that the volume of entrapped air remains constant and $\delta$ therefore becomes a function of sheet radius $R$, i.e. $\delta = V/(\pi R^2)$, where $V$ is the total volume of air entrapped, giving

$$\frac{\mathrm{d}R(t)}{\mathrm{d}t} = -C\sqrt{\pi\sigma/(\rho V)}\; R(t).$$

This predicts an exponential fall-off in sheet radius with time:

$$R(t) = R_o \exp(-C\sqrt{\pi\sigma/(\rho V)}\; t). \tag{3.1}$$

Figure 5 shows typical evolution of the air-sheet radius vs. time during the contraction. The best-fit exponential curves are also included, giving slightly varying values for $C$. For the largest impact Reynolds number, i.e. thinnest air sheet, the contraction lasts for only 60 μs. During that time, the drop will only fall 230 μm. The measured contraction speeds are consistent with the above formula and the measured thicknesses, as is demonstrated by the numeric values of $C = 0.94$ with r.m.s. variation of 0.13, shown in the inset. This value is in very good agreement with the results of Oguz & Prosperetti (1989), keeping in mind that the important radius of curvature is here determined by the thickness of the air sheet. This thickness is much smaller than the horizontal radius of the sheet, except at the end of the process where the inertia of the motion has stretched the bubble into a vertical column, which splits up into two bubbles, by Rayleigh instability. This very robust mechanism explains the curious fact that exactly two entrained bubbles are often observed, as mentioned by Esmailizadeh & Mesler (1986).

The above results imply that $We_\delta = \rho\delta U^2/\sigma \approx 1$ during the contraction, based on $\delta$, while the relevant length scale for $Re$ is the radius of the sheet $R_o$. Using the capillary velocity gives $Re = R_o\sqrt{\sigma/(\rho\delta)}/\nu \approx 1500$, showing that viscous forces are insignificant.

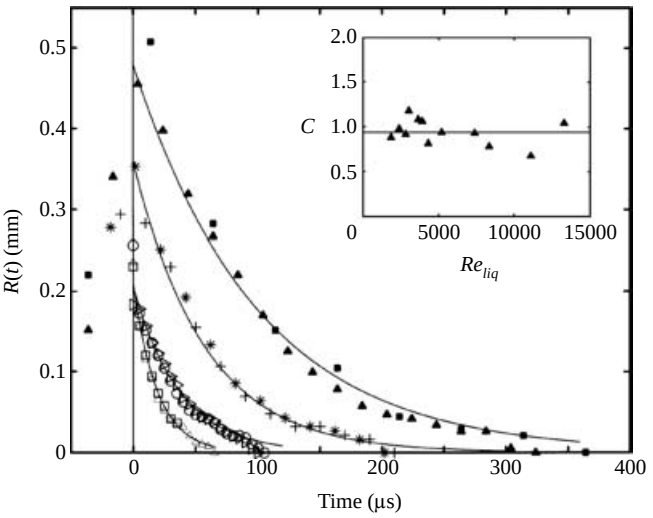


FIGURE 5. The radial contraction of the air sheet caught under an impacting water drop of diameter $D = 3.47$ mm for different impact velocities $U$. Two realizations are shown for each impact condition. The radius of the sheet goes to zero as the bubble splits in two. ■, ▲, $U = 0.69\,\mathrm{m\,s^{-1}}$ ($Re_g = 159$). ⋆, +, $U = 0.87\,\mathrm{m\,s^{-1}}$ ($Re_g = 201$). ○, ▷, $U = 3.28\,\mathrm{m\,s^{-1}}$ ($Re_g = 759$). □, △, $U = 3.84\,\mathrm{m\,s^{-1}}$ ($Re_g = 886$). The solid curves are exponential fits to the data points, based on (3.1). Inset: the best fit coefficient $C$ in (3.1) vs. liquid Reynolds number $Re_\ell$.

### 3.3. *Necklace instability*

During the contraction of the air sheet, a beautiful undulation, resembling a pearl necklace, develops along its edge. This is clearly observed in panel 3 of figure 2(*b*) and less clearly in panel 5 of figure 2(*a*).

The optical resolution allows us to study the evolution of these undulations only for the largest sheets. The undulations do not break off to form bubbles, but rather grow in amplitude and are observed to merge with their neighbours, as is indicated in figure 6(*a*). One can speculate these undulations are initiated by capillary instability of the edge of the air sheet, which is thicker (see inset in figure 6(*b*) taken from Oguz & Prosperetti 1989) and can initially be modelled by a straight cylinder of air of diameter $d \approx 2\delta_o$, where $\delta_o$ is the average initial thickness of the air sheet. The Rayleigh instability predicts a wavelength $\lambda^* = \pi d/0.484 \approx 2\pi\delta_o/0.484$, see Chandrasekhar (1961) and discussion in Weiss & Yarin (1999). Figure 6(*b*) shows the measured normalized wavelength $\lambda/(2\pi\delta/0.484)$, using the local $\delta$, versus diameter of the air sheet during its contraction. These results indicate that the initial wavelength is consistent with this type of instability, the ratio approaching 1, but as the sheet contracts the undulations stabilize and merge with adjacent undulations, the wavelength growing only slightly as the sheet thickens. The large spread in the measured $\lambda$ is principally due to the side view, which limits the number of wavelengths used in this estimate to 2–3, making merging of adjacent undulations change $\lambda$ significantly. Values of $\lambda$ from thinner sheets, where the wavelength can be measured, show similar values, see figure 6(*c*), where $\lambda/\lambda^* = 1.2 \pm 0.1$. However, larger magnifications would be needed to fully explore $\lambda$ for the thinnest sheets.

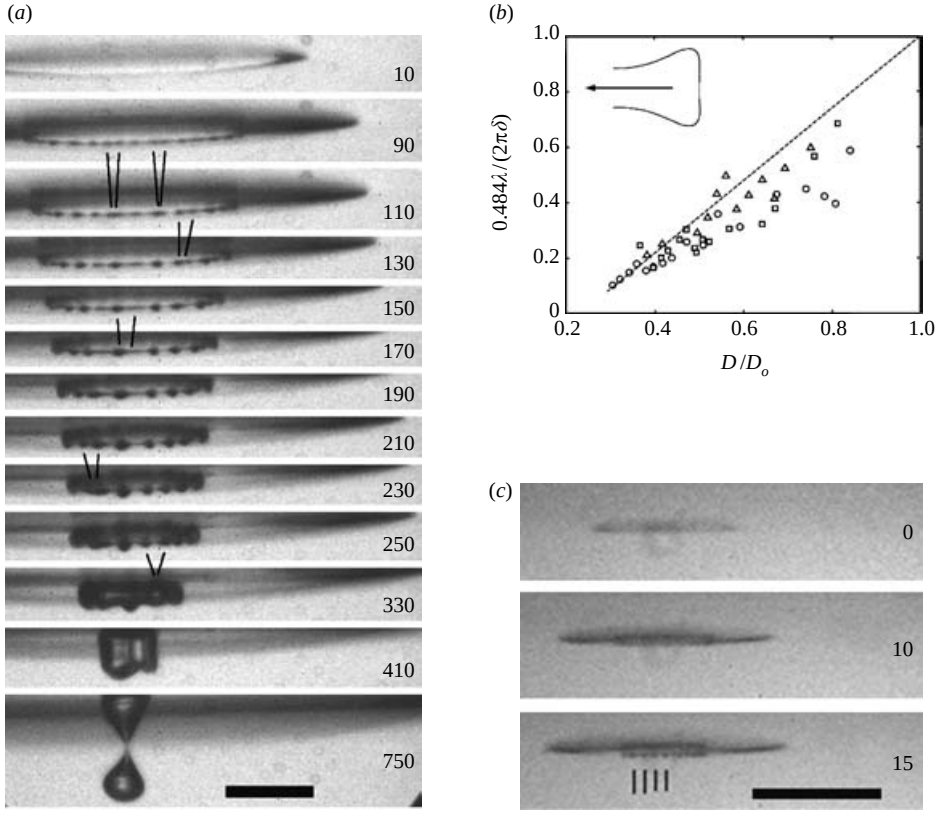


FIGURE 6. Necklace instability. (*a*) Sequence of images showing the evolution of the azimuthal undulations, for the same impact conditions as in figure 2(*b*). (*b*) The normalized average wavelength of the undulations vs. sheet diameter. Results are shown for three separate identical impacts, like the one shown in (*a*). (*c*) Azimuthal undulations for a thinner air sheet, for $We = 115$, $Re = 356$, same as figure 2(*a*). The scale bars are 500 μm long. Times listed in (*a*, *c*) are in μs from first contact.

### 3.4. *Oguz–Prosperetti bubble rings*

The Oguz–Prosperetti (1989) bubble entrapment mechanism predicts the entrapment of bubble rings at the outer contact line, which is driven outwards by capillarity. Figure 7(*a*) shows such a case, where two rings of bubbles are visible. We estimate that these particular rings contain 110 and 65 bubbles respectively, about 25 μm in diameter. Ejecta sheets (Weiss & Yarin (1999); Thoroddsen 2002) may also entrap toroidal bubbles.

The contact of the liquid surfaces, outside the main air sheet, often becomes visible as a cloudy sheet between the two main bubbles, see figure 7(*b*). This might be interpreted as myriad much smaller micron-sized bubbles, too small to resolve.

### 3.5. *Other entrapment phenomena at low We*

For low impact velocities ($We < 22$), the air sheet is thickest and large deformation of the free surface takes place before liquid contact. This produces an air sheet taking the form of a spherical cap, which leads to a variety of new entrapment phenomena, as shown in figure 8. Contact often occurs asymmetrically at the boundaries. Figure 8(*a*)

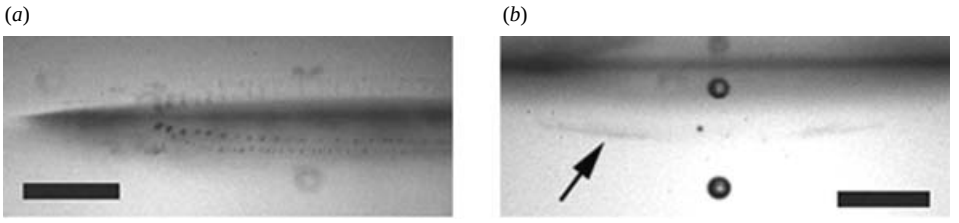


FIGURE 7. (*a*) Two outer rings of small bubbles produced by the Oguz–Prosperetti (1989) mechanism. $D = 3.47$ mm, $U = 3.84\,\mathrm{m\,s^{-1}}$ ($We = 720$, $Re_g = 886$). (*b*) The arrow marks a cloudy line of micro-bubbles between the main bubbles, generated by the outwards motion of the contact line, $D = 3.47$ mm, $U = 0.69\,\mathrm{m\,s^{-1}}$ ($We = 23$, $Re_g = 159$). The scale bars are 500 μm long.

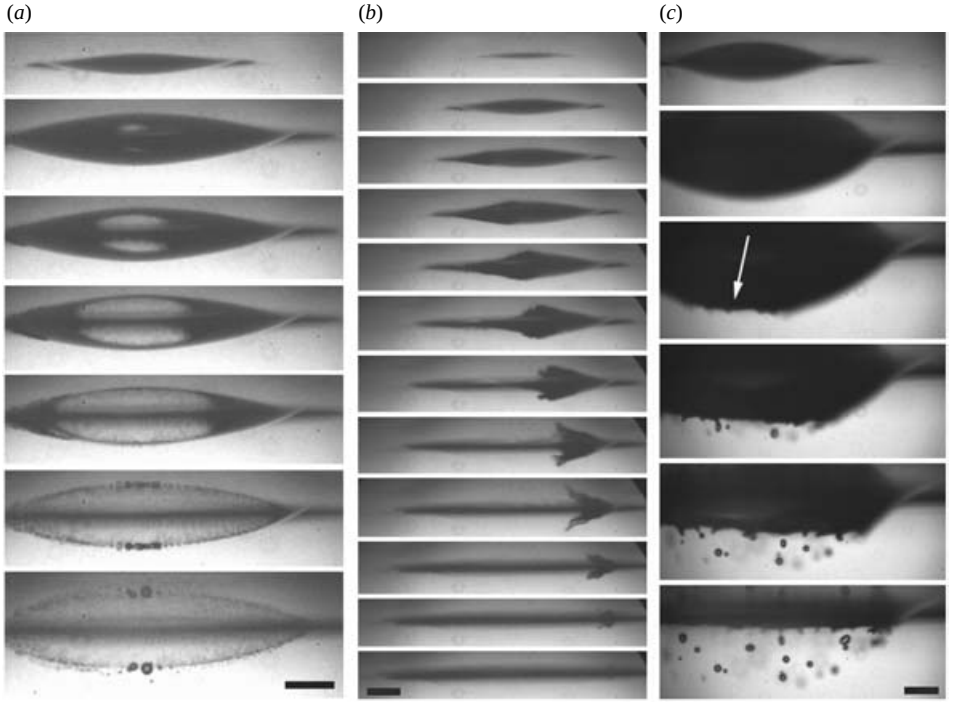


FIGURE 8. Various entrapment phenomena for low impact velocities. The thickness of the air sheets $\delta$ is estimated from their breakup speed from (3.1). (*a*) A sheet of micro-bubbles, $D = 4.24$ mm, $U = 0.60\,\mathrm{m\,s^{-1}}$, $\delta \approx 1.8$ μm ($We = 22$, $Re_g = 170$). Times are 310, 880, 910, 940, 970, 1050, 1320 μs from first contact. (*b*) Disappearing sheet of air. The edge of the air sheet is pulled from left to right. $D = 2.95$ mm, $U = 0.40\,\mathrm{m\,s^{-1}}$ ($We = 6.5$, $Re_g = 79$), $\delta \approx 7$ μm. Times shown are 100, 400 and then every 100 μs after first contact. (*c*) Sheet breaks up into numerous 'larger' bubbles about 150 μm in diameter. The arrow points to the location of the first contact, from which the breakup of the sheet propagates, similar to a bursting bubble. Times shown are 1.5 and 5.75 ms after first contact and then at 200 μs intervals. $D = 4.24$ mm, $U = 0.40\,\mathrm{m\,s^{-1}}$, ($We = 9.6$, $Re_g = 106$), $\delta \approx 8$ μm. The scale bars are 500 μm long.

shows a case where the propagating edge leaves a trail of micro-bubbles. This is most likely due to the sheet curvature which produces a component of the capillary force perpendicular to the direction of travel. Using the measured speed of propagation we can estimate $\delta$ and based on the approximate spacing of the micro-bubbles we can

estimate their size as 15 μm. On the order of 5000 bubbles are generated. The larger bubble on the centreline suggests the presence of a dimple in the air sheet. However, under slightly different impact conditions the sheet has been observed to disappear without leaving any bubbles, figure 8(*b*). This seems to occur if the drop shape leads to contact at the edge of the sheet, before it has time to thin by drainage. In figure 8(*c*) contact occurs much later and the sheet has become highly curved, now breaking up into numerous large bubbles.

For even lower impact velocities the drop can 'float' on the surface before contact is made. This leads to the 'coalescence cascade', studied by Thoroddsen & Takehara (2000), which results in repeated contact events and associated air entrapment.

## 4. Conclusions and discussion

Herein we have studied the entrapment of an air sheet by an impacting drop, measuring its thickness and describing its rapid contraction by surface tension. We have identified an azimuthal undulation along its edge and connected the amount of air entrapped to the bottom curvature of the drop as well as to the Reynolds number.

We can conclude from these results that most of the air entrapped during the impact of a raindrop will occur due to secondary droplets, such as those detached from the crown or the Worthington jet, as they impact with lower velocity. The total volume of air entrained by all these secondary drops can be roughly estimated as only 2% of the original drop volume. The local amount of rainfall can therefore be used for a rough estimate of air entrainment into the ocean by this mechanism. This does not include the bubbles trapped by the collapsing craters. Once trapped the bubbles are often carried to a few cm depth by a vortex ring generated by the capillary-driven motions at the coalescing surfaces, see e.g. Hallett & Christensen (1984), Carroll & Mesler (1981), Peck & Sigurdson (1994) and Durst (1996). They can therefore easily dissolve into the liquid. This vortex ring is most pronounced for low impact Weber numbers, likely to occur for secondary droplets, see Hsiao, Lichter & Quintero (1988).

The largest entrapped bubbles observed here were about 300 μm in diameter, see figure 2(*b*). This is somewhat smaller than the bubbles entrained by the collapse of the impact crater, Pumphrey, Crum & Bjorno (1989) and Rein (1993, 1996), but may be large enough to contribute to the underwater noise of rain.

A bubble is also caught under a drop impacting on a solid surface, as was revealed in the images of Chandra & Avidisian (1991) and Thoroddsen & Sakakibara (1998). However, we expect the contraction speeds in that case to be much slower due to the presence of the liquid–solid contact line.

S. T. T. was supported by a JSPS fellowship during his stay at Kinki University.

## REFERENCES

Blanchard, D. C. & Woodcock, A. H. 1957 Bubble formation in the sea and its meteorological significance. *Tellus* **9**, 150–158.

Carroll, K. & Mesler, R. 1981 Part II: Bubble entrainment by drop-formed vortex rings. *AIChE J.* **27**, 853–856.

Chandra, S. & Avedisian, C. T. 1991 On the collision of a droplet with a solid surface. *Proc. R. Soc. Lond.* A **432**, 13–41.

Chandrasekhar, S. 1961 *Hydrodynamic and Hydromagnetic Stability*. Clarendon.

Esmailizadeh, L. & Mesler, R. 1986 Bubble entrainment with drops. *J. Colloid Interface Sci.* **110**, 561–574.

Etoh, T. G. 1992 High speed camera of 4500 pps. *J. Inst. Television Engrs Japan* **45** No. 5, 534–545 (in Japanese).

Etoh, T. G., Poggemann, D., Ruckelshausen, A. *et al.* 2002 A CCD image sensor of 1 M frames/s for continuous image capturing of 103 frames. *2002 IEEE Intl Solid-State Circuits Conf. Digest of Technical Papers, Visuals Supplement, 30-31*, vol. 386, pp. 46–47.

Foote, G. B. 1975 The water drop rebound problem: Dynamics of collision. *J. Atmos. Sci.* **32**, 390–402.

Durst, F. 1996 Penetration length and diameter of vortex rings generated by impacting water drops. *Exps. Fluids* **21**, 110–117.

Gopinath, A. & Koch, D. L. 2002 Collision and rebound of small droplets in an incompressible continuum gas. *J. Fluid Mech.* **454**, 145–201.

Hallett, J. & Christensen, L. 1984 Splash and penetration of drops in water *J. Rech. Atmos.* **18**, 225–242.

Hsiao, M., Lichter, S. & Quintero, L. G. 1988 The critical Weber number for vortex and jet formation for drops impinging on a liquid pool. *Phys. Fluids* **31**, 3560–3562.

Jiang, Y. J., Umemura, A. & Law, C. K. 1992 An experimental investigation on the collision behaviour of hydrocarbon droplets. *J. Fluid Mech.* **234**, 171–190.

Nobari, M. R., Jan, Y.-J. & Tryggvason, G. 1996 Head-on collision of drops – A numerical investigation. *Phys. Fluids* **8**, 29–42.

Oguz, H. N. & Prosperetti, A. 1989 Surface-tension effects in the contact of liquid surfaces. *J. Fluid Mech.* **203**, 149–171.

Peck, B. & Sigurdson, L. 1994 The three-dimensional vortex structure of an impacting water drop. *Phys. Fluids* **6**, 564–576.

Prosperetti, A. & Oguz, H. 1993 The impact of drops on liquid surfaces and the underwater noise of rain. *Annu. Rev. Fluid Mech.* **25**, 577–602.

Pumphrey, H. C., Crum, L. A. & Bjorno, L. 1989 Underwater sound produced by individual drop impacts and rainfall. *J. Acoust. Soc. Am.* **85**, 1518–1526.

Rein, M. 1993 Phenomena of liquid drop impact on solid and liquid surfaces. *Fluid Dyn. Res.* **12**, 61–93.

Rein, M. 1996 The transitional regime between coalescing and splashing drops. *J. Fluid Mech.* **306**, 145–165.

Rother, M. A., Zinchenko, A. Z. & Davis, R. H. 1997 Buoyancy-driven coalescence of slightly deformable drops. *J. Fluid Mech.* **346**, 117–148.

Thoroddsen, S. T. 2002 The ejecta sheet generated by the impact of a drop. *J. Fluid Mech.* **451**, 373–381.

Thoroddsen, S. T. & Sakakibara, J. 1998 Evolution of the fingering pattern of an impacting drop. *Phys. Fluids* **10**, 1359–1374.

Thoroddsen, S. T. & Takehara, K. 2000 The coalescence cascade of a drop. *Phys. Fluids* **12**, 1265–1267.

Weiss, D. A. & Yarin, A. L. 1999 Single drop impact onto liquid films: neck distortion, jetting, tiny bubble entrainment, and crown formation. *J. Fluid Mech.* **385**, 229–254.